Journal of Alloys and Compounds 899 (2022) 163192

Contents lists available at ScienceDirect

Journal of Alloys and Compounds

journal homepage: www.elsevier.com/locate/jalcom

Research Article

$MnFe_2O_4$ nano-flower: A prospective material for bimodal hyperthermia

S.K. Shaw[a], J. Kailashiya[b], Santosh K. Gupta[c,e], C.L. Prajapat[d,e], Sher Singh Meena[f], D. Dash[b], P. Maiti[g], N.K. Prasad[a,*]

[a] Department of Metallurgical Engineering, Indian Institute of Technology (Banaras Hindu University), Varanasi 221005, India
[b] Center for Advanced Research on Platelet Signaling and Thrombosis Biology, Department of Biochemistry, Institute of Medical Sciences, Banaras Hindu University, 221005, India
[c] Radiochemistry Division, Bhabha Atomic Research Centre, Mumbai 400085, India
[d] Technical Physics Division, Bhabha Atomic Research Centre, Mumbai 400085, India
[e] Homi Bhabha National Institute, Anushaktinagar, Mumbai 400094, India
[f] Solid State Physics Division, Bhabha Atomic Research Centre, Mumbai 400085, India
[g] School of Materials Science and Technology, Indian Institute of Technology (Banaras Hindu University), Varanasi 221005, India

ARTICLE INFO

Article history:
Received 11 August 2021
Received in revised form 21 November 2021
Accepted 7 December 2021
Available online 9 December 2021

Keywords:
Magnetic materials
Nanoflower
Magnetic hyperthermia
Photothermia
$MnFe_2O_4$

ABSTRACT

Magnetic nanoparticles (MNPs) have emerged as efficient materials for thermo-therapeutic modalities viz. magnetic fluid hyperthermia (MFH) and photo-thermal therapy (PTT). Nevertheless, the quest to further enhance the effectiveness of such materials is a major challenge to their successful endeavour. In the present work, we have synthesised $MnFe_2O_4$ nano-flowers utilising solvo-thermal method to be employed as nano-heat generators during MFH and PTT. The material, in addition to effective heating under an alternating magnetic field (AMF), demonstrated impressive heating ability under near infra-red (NIR) irradiation. Various techniques, such as, X-ray diffraction (XRD), transmission electron microscopy (TEM), X-ray photo-electron spectroscopy (XPS) and Mössbauer spectroscopy were used to study the structural features and chemical composition of the sample. The photoluminescence spectroscopy (PLS) has further corroborated the efficient heating behaviour of the sample under NIR irradiation. The observed intrinsic loss power value of 5.31 ± 0.079 nH m^2 kg^{-1} is significantly higher than the commercially available ferro-fluids and comparable to previously reported values for iron oxide nano-flowers. A substantial SiHa cells death during photo-thermal treatment was noticed at a concentration of 500 μg/mL of $MnFe_2O_4$ nano-flowers after exposure to 808 nm laser of 0.66 W cm^{-2} power density for only 10 min. However, at the same concentration of nanoflowers (i.e. 500 μg/mL) and exposure time (i.e. 10 min) during MHT with SiHa cells, a significant decrease in cell viability was not observed.

1. Introduction

Despite the various progress and introduction of cutting edge technologies in medical sciences, cancer remained a global and significant public health concern. More than 600,000 people, alone in the United States, lose their battle against this deadly disease every year [1]. Nevertheless, its increasing burden in a populous country like India is a grim matter of concern and must be checked in time [2].

The traditional treatment methods, such as chemotherapy and radiotherapy, are less efficient and can cause severe collateral damage to healthy body tissues deteriorating the condition of the patients [3,4]. Thus, effective treatment methodologies which selectively kill cancer cells or tissues are in demand all the time in global arena. Among several strategies, localised treatment have emerged as one of the most promising methodology for cancer therapy employing either magnetic nanoparticles (MNPs) in magnetic fluid hyperthermia (MFH) or photo-sensitive nanoparticles in photo-thermal therapy (PTT) [5].

These localised treatment modalities depend on the capability of nanoparticles (NPs) to emit heat, which is utilised in the destruction of cancer cells, under the application of a distant energy source [5]. Iron oxide nanoparticles (IONPs) owing to their excellent biocompatibility are considered the most suitable candidate for MFH [6,7] and render them as prospective material for several bio-applications including drug delivery [8], magnetic targeting [9], cell separation [9], magnetic resonance imaging [10] and magnetic particle imaging [11]. Moreover, their unique magnetic property allows

* Corresponding author.
E-mail address: nandkp.met@iitbhu.ac.in (N.K. Prasad).

https://doi.org/10.1016/j.jallcom.2021.163192
0925-8388/

them to be remotely controlled and guided to a specific site (tumour region) using a magnet to provide an on-demand toxic amount of heat by applying a high frequency alternating magnetic field (AMF) [12]. When triggered with an AMF, the heat is released due to hysteresis losses which arise from phase delay in magnetisation response of the material to the applied AMF [13]. The heat released can be improved by increasing the area under the A.C. hysteresis loop, which depends on the saturation magnetisation and coercive field of magnetic nanoparticles (MNPs) [13,14].

Usually, small super-paramagnetic IONPs were favoured for MFH because of their non-interacting behaviour in the absence of any magnetic field and longer life-time in blood circulation [15]. However, the super-paramagnetic IONPs are limited by relatively low saturation magnetisation and coercive field values, restricting their heating efficiency during the treatment [16]. It will thus necessitate a large amount of materials, in case of super-paramagnetic IONPs, to produce sufficient heat for the effective destruction of cancer cells. However, to reduce the possible toxic effect associated with foreign particles, the usage of a minimal amount of MNPs for MFH is highly advantageous and demand of the time. It could be achieved using magnetic materials with high intrinsic loss power (ILP, a parameter which express the heating efficacy) value [17]. With high ILP values materials, a low amount would be required to attain the therapeutic temperature even at low field intensity and frequency. Moreover, it could also aid in the likelihood of handling metastatic malignance where the accumulation of MNPs is relatively low.

In the past few years various strategies, which aim at enhancing the saturation magnetisation and anisotropy of the material have been suggested to improve the heating behaviour. It includes modifying the size, shape, structure and chemical composition of the IONPs [18–22]. One specific structure, magnetic nano-flowers (MNFs) of iron oxide, is quite stirring as they have shown outstanding heating performance during MFH [23,24]. In addition, various other MNPs have been also evaluated and were found to display effective heating during MFH [25]. $MnFe_2O_4$ nanoparticles, in particular, have displayed heating and biocompatibility in line with IONPs [26]. We believe their heating performance could further be increased with nano-flower morphology as witnessed for iron oxide nano-flowers over iron oxide mono-core particles [27].

The co-operative magnetic interaction among the cores, which physically adhere together to give rise a flower-like pattern, leads to a modified magnetic state within the nano-flowers such as enhanced saturation magnetisation (M_S) and initial susceptibility [25,28]. The modified magnetic interactions in turn enhances the heating performance during MFH [25–29]. MNFs also mitigate the limitation associated with bigger mono-core particles, which often require AMF of higher field intensity to overcome the anisotropy barrier for effective heating [18]. A lower field intensity is highly desirable to avoid the possibility of eddy current heating inside the body. With the nano-flowers of comparable or even bigger size than the mono-core particles, effective heating could be produce at a relatively lower field intensity [29,30]. In addition to the exceptional contribution of IONPs in localised cancer therapy via MHF, some recent reports pointed out their potential application in PTT, which attracted the significant interest of the research community [5,31].

The PTT is centred on nanoparticles' ability to translate the electromagnetic radiation of near-infrared (NIR) wavelength to heat for the destruction of cancer cells [5]. Various photo-sensitive nanomaterials, such as gold [32], carbon nanotubes [33] and graphene [34] have been studied to explore their ability to generate heat during PTT. However, the clinical utilisation of these materials is limited by their non-specific distribution in normal tissues decreasing the accumulation of the photo-thermal agents in tumour sites and the potential in-vivo toxicity associated with non-biodegradable and bio-persistent behaviour [35,36]. Recently, IONPs have demonstrated effective heating behaviour during PTT and that too at a much lower amount generally required during MFT [30,31,37]. Thus, biocompatible IONPs can substantiate as an effective photothermal material mitigating the limitations mentioned above. Moreover, a combined exposure of AMF and NIR irradiation can effectively enhance their heating output [31]. However, only a few reports are available on the heating effect of IONPs under NIR irradiation, and much of them were evaluated at higher power density than recommended for human use. A rigorous study is required to realise a high-performance MNPs which can effectively release heat under NIR irradiation of low power density, in addition to MFH.

The heating effect of IONPs under NIR irradiation is due to the non-radiative recombination of the electron-hole pair during the relaxation process, causing the generation of phonons [5]. This upsurge the vibrational state of the system and hence a subsequent temperature rise. Thus, introducing a more defect state in the material might improve the heating by increasing non-radiative electron-hole recombination frequency [30,38]. In the current effort, we have assessed the heating performance of manganese ferrite nano-flowers (MF) by exposing them to AMF during MFH and NIR irradiation for PTT. We choose nano-flower structure not only for its outstanding performance during MFH but also in PTT over single-core particles [39,40]. To our knowledge $MnFe_2O_4$ nano-flowers have not been gauged for their performance in MFH or PTT to date. In the present work, we have obtained highly-crystalline MF through solvothermal reaction. The material, in addition to effective heating under an alternating magnetic field (AMF), demonstrated impressive heating ability under near infra-red (NIR) irradiation. We have systematically studied the sample's structural and magnetic properties and strained to correlate them with their heating performance during MFH and PTT.

The experimental details of this work is elaborated in Supplementary information file with materials, synthesis, magnetic ferro-fluid, instrumental related information and in-vitro studies mentioned in ESI as information item S1–S5 respectively.

2. Results and discussion

The room temperature x-ray diffraction pattern obtained for MF nano-flowers is shown in Fig. 1. The pattern suggests the formation of single-phase material with the cubic crystal structure, *Fd*-3*m* space group. The peaks were observed at 18.3°, 30.1°, 35.4°, 37.1°, 43.1°, 53.4°, 56.9°, 62.5°, 70.9° and 73.8°, corresponding to planes (111), (220), (311), (222), (400), (422), (333), (440), (620) and (533) and were assigned to the crystallographic planes of $MnFe_2O_4$, using reference JCPDS no. 74-2403. Further, we have refined the pattern

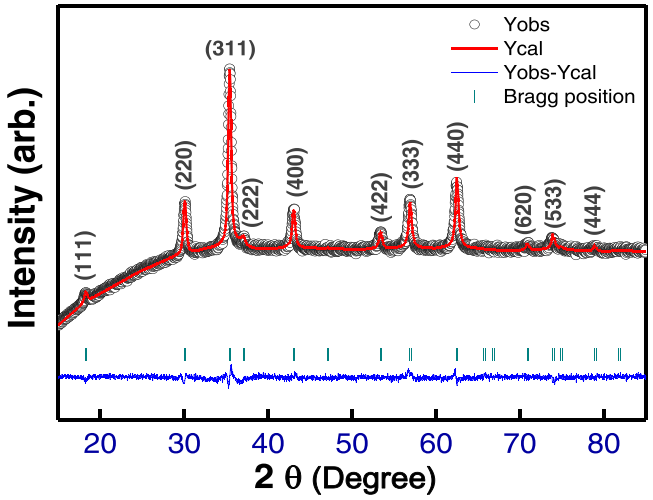

Fig. 1. Rietveld refined XRD pattern of the prepared MF sample.

Table 1
Parameters obtained from room temperature Mössbauer spectrum of powder MF sample.

Site	Hyperfine field (H_f), T ± 0.01	Isomer shift (δ) mm/s ± 0.01	Quadruple splitting (Δ) mm/s ± 0.02	Outer line width (Γ) mm/s	Relative area (RA) ± 0.03%	X2
Sextet A	48.63	0.286	0.019	0.470	29.70	
Sextet B1	46.53	0.328	-0.026	0.6598	37.96	1.208
Sextet B2	42.78	0.358	-0.039	1.104	32.31	

using FullProf software. For the refinement, we have used the initial site occupancy values considering the structure $(Mn_{0.406}Fe_{0.594})[Mn_{0.594}Fe_{1.406}]O_4$, which was derived from Mossbauer spectroscopy (Table 1). The parameters defining the goodness of fit, i.e. R_{wp}, R_e and Chi^2, were converged to 13.5, 13.2 and 1.04, respectively, after the refinement. The lattice parameter (a = 8.40 Å) obtained after Rietveld refinement was lower than that of the bulk sample (a = 8.51 Å), which could be attributed to alternate cationic distribution leading to a different degree of inversion from the bulk [41]. The approximate crystallite size calculated using Scherer's equation considering (311) peak was ~ 22 nm, which was higher than that of obtained from the refinement (~ 19 nm). Table S1 (supplementary file) lists all the parameters obtained after the Rietveld refinement.

The bright-field TEM micrograph depicts a chain-like arrangement for these nanoparticles (Fig. 2*a*). The inset of the figure captured at higher magnification clearly shows the formation of a flower-like morphology. The smaller core were adhered together to give the desired flower pattern. The average size of the flowers was observed to be ~ 42 nm with a standard deviation of 5 nm. The SAED pattern obtained was due to the planes of a spinel structure and indicates the formation of a crystalline structure, supporting the X-ray diffraction analysis.

The SEM-EDS spectrum confirmed the presence of Mn, Fe and O elements with atomic percentage of ~ 13%, 24% and 63%, respectively, in the sample. The SEM micrograph and the respective elemental mapping, acquired from the Kα energy of Mn, Fe and O, of the nano-flowers are represented in Fig. S1 (Supplementary file). Thermo gravimetric analysis (TGA) was performed in 30 – 600 °C temperature range to estimate the amount of adsorbed chemical species on the nano-flowers obtained through solvothermal method as describe in the experimental section (Information S2, Supplementary file). The TGA curve (Fig. S2) mainly revealed a two stage weight loss during the heating process. The first weight reduction, of ~ 3%, started just above the initial measurement temperature to just above 200 °C. This reduction might be associated with the evaporation of physically adsorbed water molecule and low boiling solvent complexes attached to the surface of nano-flowers [42,43]. Above this temperature a further weight reduction of ~ 4.5% was noticed up to the measuring temperature of 600 °C. This could be due to the decomposition of chemically adsorbed species (solvent) and PVP [43]. Thus, overall a reduction of ~ 7.5% in weight was witnessed by TGA experimentation. It can be kindly noted that the decrease in weight observed by TGA has not been included in the calculation of other material's properties.

We have performed the XPS analysis of MF sample in order to check the oxidation states of the elements present in the sample. The high-resolution XPS scans of Fe 2p, Mn2p, Fe3p, O1s and C1s are shown in Fig. 3 *(a–e)*, respectively. The Fe 2p XPS spectrum was split into Fe $2p_{3/2}$ and Fe $2p_{1/2}$ orbitals having peaks at 711.20 and 724.56 eV, respectively, due to spin-orbit coupling. The spectrum displayed the existence of a satellite peak around 719.25 eV which was separated by 8.05 eV from the Fe $2p_{3/2}$ peak. These data suggest that the Fe 2p spectrum was due to the Fe^{3+} ionic state [44,45]. The oxidation state of Fe was also confirmed from the Fe 3p XPS spectrum. In a study, Yamashita et al. [44] had found the Fe 3p peak position at 55.6 eV (S.D = 0.04) and 53.7 eV (S.D = 0.03) for Fe^{3+} and Fe^{2+} states respectively. In the Fe 3p spectrum obtained for the MF sample, we observed a peak around 55.2 eV, which could be due to the Fe^{3+} ionic state. The absence of any peak around 53.7 eV in the spectrum suggests that only Fe^{3+} ions were present in the sample. Further, the Fe 2p XPS spectrum was de-convoluted with the help of five sub-peaks. The peaks at 710.9 (724.23) eV and 713.4 (726.5) eV were assigned to Fe^{3+} from octahedral (o) and tetrahedral (t) sublattices respectively [46,47].

The Mn 2p XPS spectrum for the sample indicates the presence of a multivalent ionic state for Mn. The peaks at 640.12 (652) eV, 641.4 (653.18) eV and 642.64 (654.4) eV were assigned to Mn^{2+}, Mn^{3+} and Mn^{4+} ionic states respectively [48,49]. The XPS spectrum for O 1s

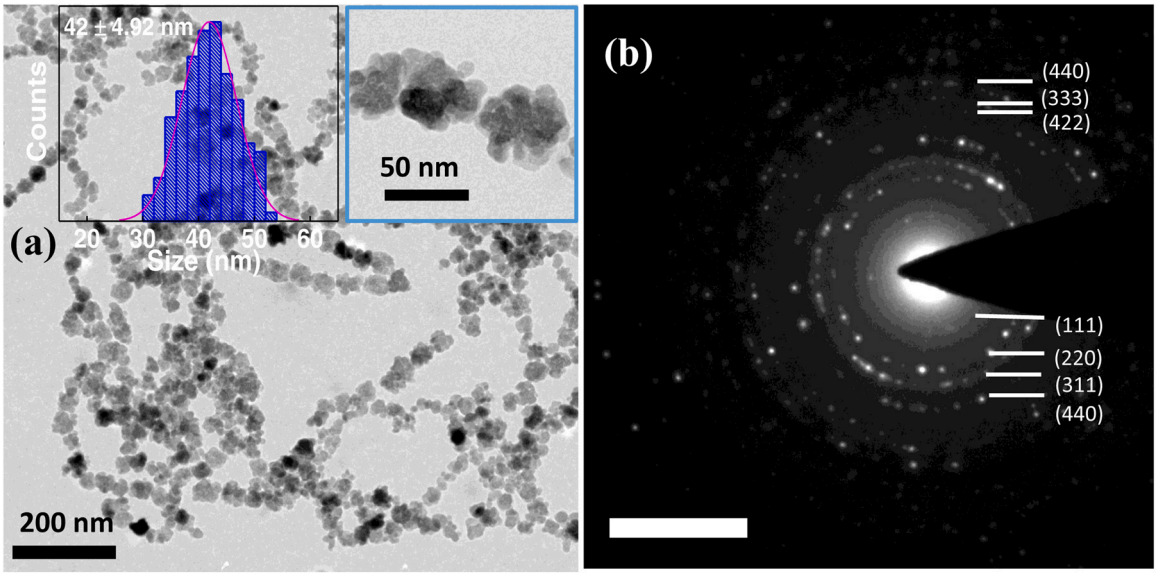

Fig. 2. (a) Bright-field TEM image (the insets show the size distribution profile and morphology at higher magnification) and (b) SAED pattern for MF sample.

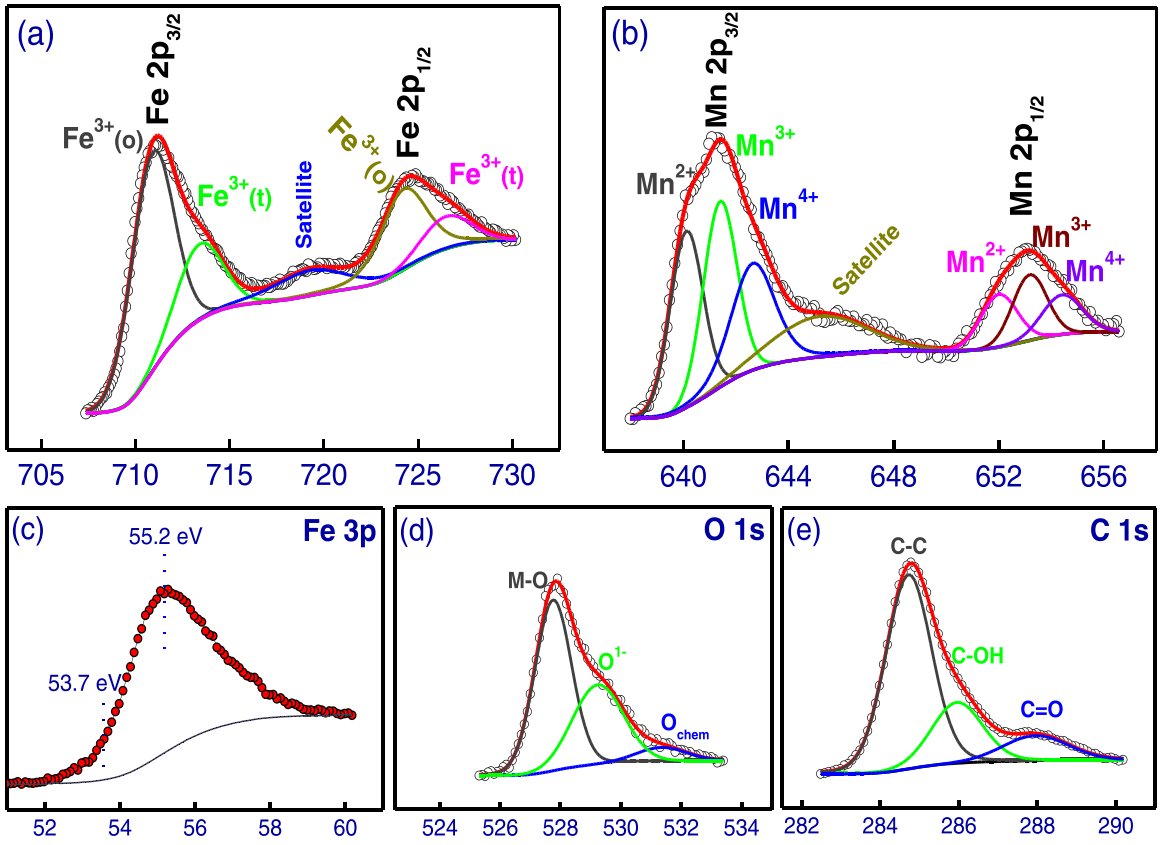

Fig. 3. High-resolution XPS spectra for (a) Fe 2p, (b) Mn 2p, (c) Fe 3p, (d) O 1s and (e) C 1s core-levels.

was de-convoluted with three peaks positioned at 529.75, 531.24, and 533.35 eV, which corresponded to metal ions oxygen bonds, surface-adsorbed oxy-hydroxide and chemically adsorbed H_2O at the surface, respectively [49].

The room temperature (RT, 300 K) Mössbauer spectrum obtained for sample MF without the application of an external field is shown in Fig. 4, and the corresponding parameters obtained after the least-square fitting of the experimental data are given in Table 1. Interestingly, we could observe a well resolved magnetically split absorption lines, which suggests that the particles were magnetically ordered and a ferri-magnetic like behaviour existed for the sample at RT [50]. The existence of only magnetically split lines in the spectrum also indicates that the blocking temperature of all the particles

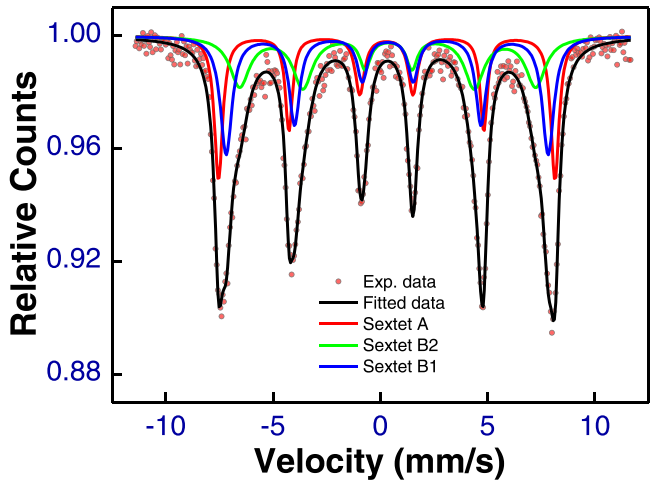

Fig. 4. Room temperature Mössbauer spectrum of powder MF sample.

was higher than 300 K. The spectrum was well fitted with three Zeeman sextets, one for tetrahedral (A) and two for octahedral (B) sites [51]. The values of the isomer shift which were found between 0.2864 and 0.358 mm/s, suggest that all Fe ions were in Fe^{3+} high spin state [52], validating the findings of XPS spectroscopy. The sextet-A showing smaller isomer shift represents Fe^{3+} ions at A site, and it also exhibited the highest hyperfine field. The other two sextets, i.e. sextet B1 and B2 with relatively larger isomer shifts, characterise Fe^{3+} ions at two different environments in B-site [51,53].

Fig. 5*a* and *b* show the hysteresis loop recorded up to ± 50 kOe at 300 K and a temperature-dependent magnetisation behaviour from 5 K to 300 K, measured under ZFC and FC conditions at a static magnetic field of 250 Oe, respectively. As apparent from the room temperature DC magnetometry M-H curve (Fig. 5*a*), an early saturation in magnetisation was attained for these nano-flowers. The saturation magnetisation (M_S) value was observed to ~ 75 emu/g for MF, which was close to the bulk magnetisation value (~ 83 emu/g) for $MnFe_2O_4$ [41]. The high M_S value could be due to the reduced surface disorder and an enhanced magnetic ordering within the nano-flowers, a constructive aspect of such a structure. This could be appreciated from the reported M_S values for single-core nanoparticles of comparable sizes, which were relatively lower than for the present nano-flower [41,51]. The sample displayed a finite coercive field (H_C) of ~ 15 Oe and remanent magnetisation (M_r) of ~ 3 emu/g as depicted from the inset of Fig. 5*a*.

The temperature-dependent magnetisation behaviour (5–300 K) for MF in ZFC and FC condition with an applied field of 250 Oe displayed remarkable behaviour. The curves showed an irreversible behaviour right from 300 K down to the lowest measurement temperature of 5 K. The irreversibility, or in other words, the bifurcation between the ZFC and FC curves was getting larger on decreasing the temperature, which, directs to the presence of higher magnetic anisotropy field. The ZFC curve displayed a continuous increase in

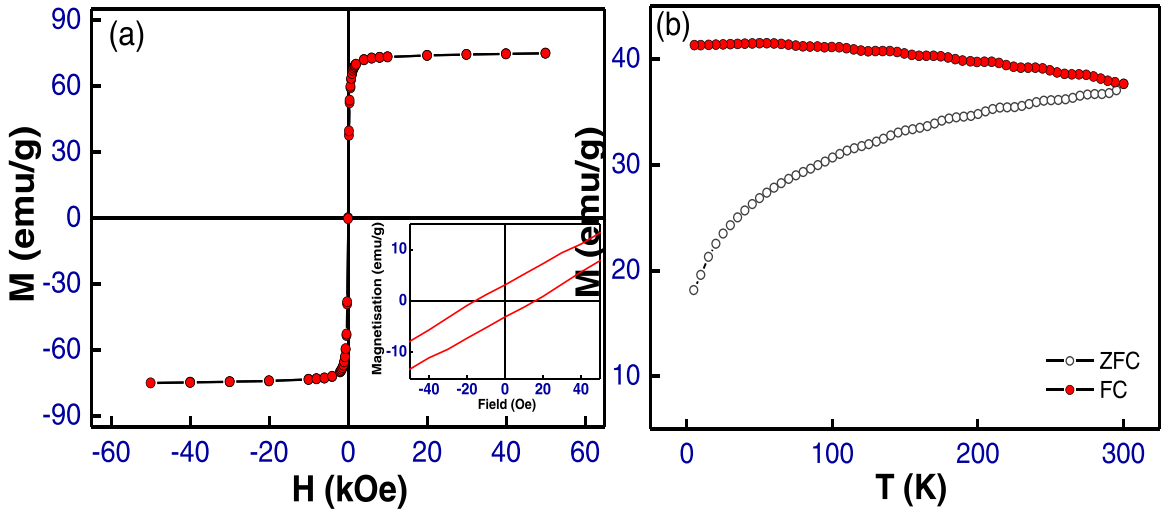

Fig. 5. (a) Room temperature magnetisation vs. field curve and (b) temperature dependent (5–300 K) magnetic behaviour (ZFC-FC) for powder MF sample.

magnetisation on increasing the experimental temperature from 5 to 300 K. The absence of any peak in the ZFC magnetisation curve indicates that the particles were essentially in the magnetically blocked condition up to room temperature, supporting the findings of Mössbauer spectroscopy [50]. The FC curve depicts a typical characteristic of material with strong magnetic inter-particle or di-pole-dipole interaction [30,50]. This interaction may be the reason for the chain-like assembly observed in bright-field TEM micro-graph. Such an interaction, depending on the characteristics of an individual particle and the AMF parameters, can either enhance or impair the MHT performance [54,55]. In clusters of nano-flowers, the existence of supraferromagnetic interaction enhances the heating performance during MHT [56].

The aqueous ferro-fluid showed good stability as observed from the zeta potential (ζ) measurement. The mean ζ values were quantified as 13.33 ± 0.25, − 1.96 ± 0.58, − 31.43 ± 0.95 and − 36.67 ± 0.61 at 2, 4, 6 and 8 pH values, respectively (Fig. S3b). The dynamic light scattering plot (Fig. S3a) depicted a uni-modal distribution of hydrodynamic size (D_h) for the MF particles dispersed in the aqueous ferrofluids. The mean D_h value was observed to be 81 ± 1.06, which was higher than the particle's size observed in TEM as expected, as the former display the hydrodynamic radius value.

Fig. 6*a* shows the increase in temperature of aqueous ferro-fluids of concentration 2 mg/mL after exposing them to AMF of different field intensities and frequencies. The temperature elevation curves were plotted by taking the average of three readings. As can be observed from the graph, the ferro-fluid displayed a continuous increase in temperature but with dissimilar rates at different applied AMFs. For example, it took an average time of ~ 465 s to reach the therapeutic temperature (~ 42 °C) when exposed to an AMF of amplitude 110 Oe and frequency 466 kHz while the same has been achieved in only ~ 175 s at 170 Oe and 330 kHz.

The heating behaviour of magnetic nanoparticles is believed to vary with amplitude and frequency of applied AMF as H^2 (constant *f*) and *f* (constant H) in the regime of linear response theory [57]. But as witnessed from the temperature-dependent magnetisation behaviour, these nano-flowers were in a ferri-magnetically blocked state, so a deviation from a simple H^2 behaviour is likely to be expected [14]. Though with the limitation of the equipment used, it is not possible to evaluate the heating behaviour at the varying field with constant frequency and vice-versa, a qualitative evaluation is still possible. At the AMF of amplitude 170 Oe, the ILP value has increased from 2.44 ± 0.048 to 3.79 ± 0.057 nH m^2 kg^{-1} by increasing the frequency of AMF from 165 to 330 kHz.

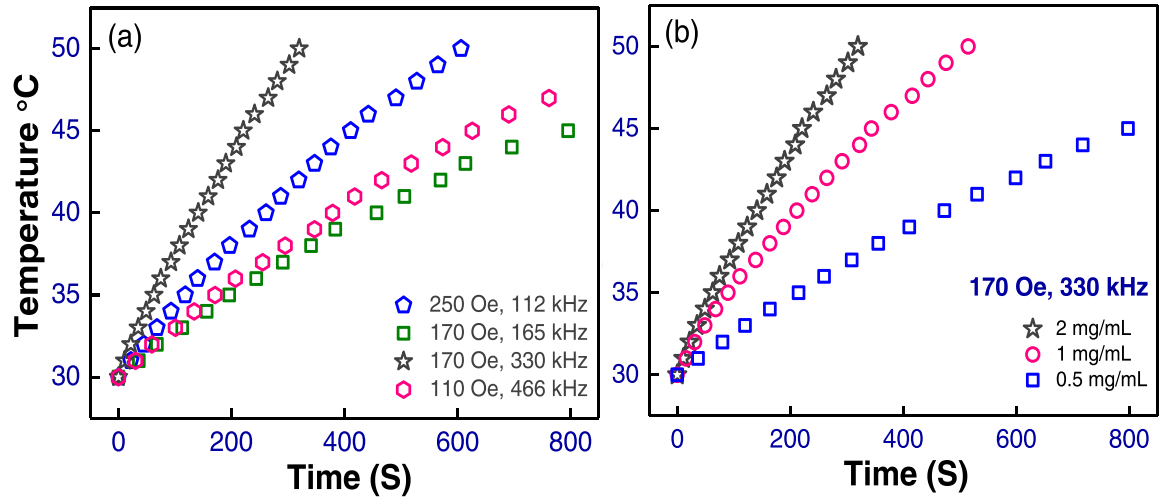

Fig. 6. (a) Field intensity and frequency dependent temperature rise curves with time for aqueous ferro-fluids of concentration 2 mg/mL, and (b) concentration dependent temperature rise curves at the AMF of 170 Oe, 330 kHz.

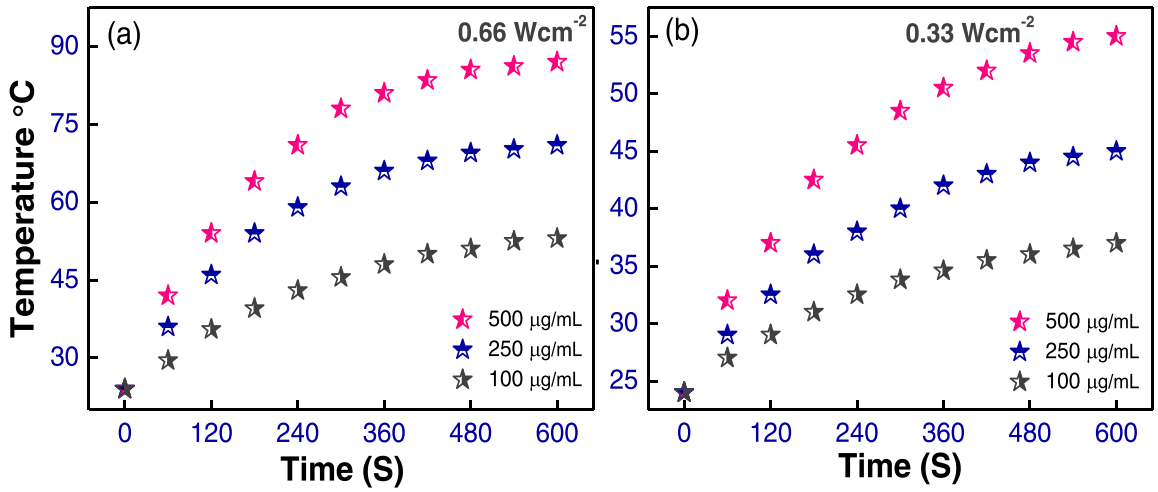

Fig. 7. Concentration dependent heating behaviour of aqueous suspension of MF when exposed to NIR laser of wavelength 808 nm of (a) 0.66 W cm^{-2} and (b) 0.33 W cm^{-2} power density.

An increased frequency tends to enhance the M-H loop's hysteresis area during the dynamic magnetisation process, which is a direct measurement of heat dissipated (temperature rise) during MHT [58]. The ILP value was 2.76 ± 0.056 and 2.38 ± 0.059 nH m^2 kg^{-1} at 250 Oe, 112 kHz and 110 Oe, 466 kHz, respectively. While 250 Oe was the highest field intensity utilised in the experiment, the maximum in ILP was not achieved due to the lower field frequency associated with it. Again at the highest field frequency, 466 kHz, the associated field intensity was lowest (110 Oe), which might not be sufficient to rotate the maximum moment in its direction and hence lower heating was noticed [14,18]. The heating behaviour could further be enhanced by increasing the magnitude of AMF, as the anisotropy field of the sample was higher (suggested by ZFC/FC magnetisation) than the field intensity used in the hyperthermia experiment. However, of all AMFs applied, we have observed the maximum heating of MF ferro-fluid at 170 Oe and 330 kHz, so we further decided to evaluate a concentration-dependent heating behaviour at the same AMF. As the inter-particle and dipolar interactions are present in our sample, the heating behaviour is expected to vary with concentration [14,29,30].

Fig. 6*b* shows the temperature elevation profile of MF ferro-fluids of different concentration at 170 Oe and 330 kHz. As observed from the curves, the efficiency of heating improved at a lower concentration. The ferro-fluid displayed the highest ILP of 5.31 ± 0.079 at the concentration of 1 mg/mL. This value is lower than that obtained for γ-Fe_2O_3 nano-flowers [30], but comparable to that of Fe_3O_4 nano-flowers [23]. The respective ILP values at the concentrations of 2 and 0.5 mg/mL were 3.79 ± 0.057 and 4.44 ± 0.053 nH m^2 kg^{-1}, respectively. The observed variation in ILP of the ferro-fluid could be explained through the effective anisotropy modified due to concentration variation. An increased concentration is connected with the enrichment of magnetic dipolar interactions and cluster formation, which tend to increase the system's effective anisotropy [54,55,59]. Thus, the increased effective anisotropy might have restricted a more part of the magnetisation reversal in field direction at a higher concentration. It could lead to a decrease in area under the hysteresis lowering the heat output. In hyperthermia, the final aim of all modifications, such as shape, size, concentration or field and frequency, is to make the anisotropy of the material close to the amplitude of the field applied in order to maximise the heating behaviour [14,18]. The concentration of 1 mg/mL might have provided the right condition and hence achieved maximum ILP. AC magnetometry experiments could further be used for the exact explanation of such behaviour.

We have plotted the temperature elevation curves for aqueous suspension of MF of different concentrations when irradiated with NIR laser of wavelength 808 nm of power density 0.66 and 0.33 W/cm^2 in Fig. 7*a* and *b* respectively. The temperature rise was observed to be dependent on the concentration of the aqueous suspension and the power density of the NIR laser. For instance, after the exposure to the NIR of 0.66 W/cm^2 for 10 min, the temperature reached ~ 87, 71 and 53 °C (initial temperature was 19 °C) for the aqueous suspension of concentration 500, 250 and 100 µg of material per mL, respectively. The temperature achieved after NIR irradiation of aqueous suspension of concentration 500 µg/mL was higher than that achieved by applying AMF for the same period of time. Even with the higher concentration (i.e. 2 mg/mL) the temperature raised by ~ 20 °C after 5 min of AMF exposure, whereas a rise of ~ 55 °C in temperature was observed after NIR exposure over the same period of time. The specific loss power (SLP) was observed to be dependent on the concentration and decreased with increased concentration of aqueous suspension. For example, the SLP values obtained with 0.66 W cm^{-2} power density for 500, 250 and 100 µg/mL aqueous suspension were ~ 2520, 3360 and 3864 W g m^{-1}, respectively. The values further decreased to ~ 1117, 1344 and 2100 W g m^{-1} for 500, 250 and 100 µg/mL aqueous suspension by lowering the power density of the NIR laser light to 0.33 W cm^{-2}. Overall, a better heating was witnessed with NIR laser irradiation and the maximum in SLP value was almost an order higher than that observed with AMF exposure (highest SLP ~ 320 W g m^{-1}). The DI water under the same condition displayed a temperature rise of ~ 2 °C, which confirms that the heating was essentially due to the MF particles. While, lowering the NIR laser's power density to 0.33 W/cm^2 resulted in a drop in the temperature achieved after the same period of exposure. At this power density, no obvious temperature increment (~ 1 °C) was observed for the DI water. It is well known that the non-radiative recombination of the electron hole-pair (during the relaxation from excited sate) is responsible for the generation of phonons which upsurge the vibrational state of the system leading to heat release and a subsequent temperature rise [5,38]. The non-radiative

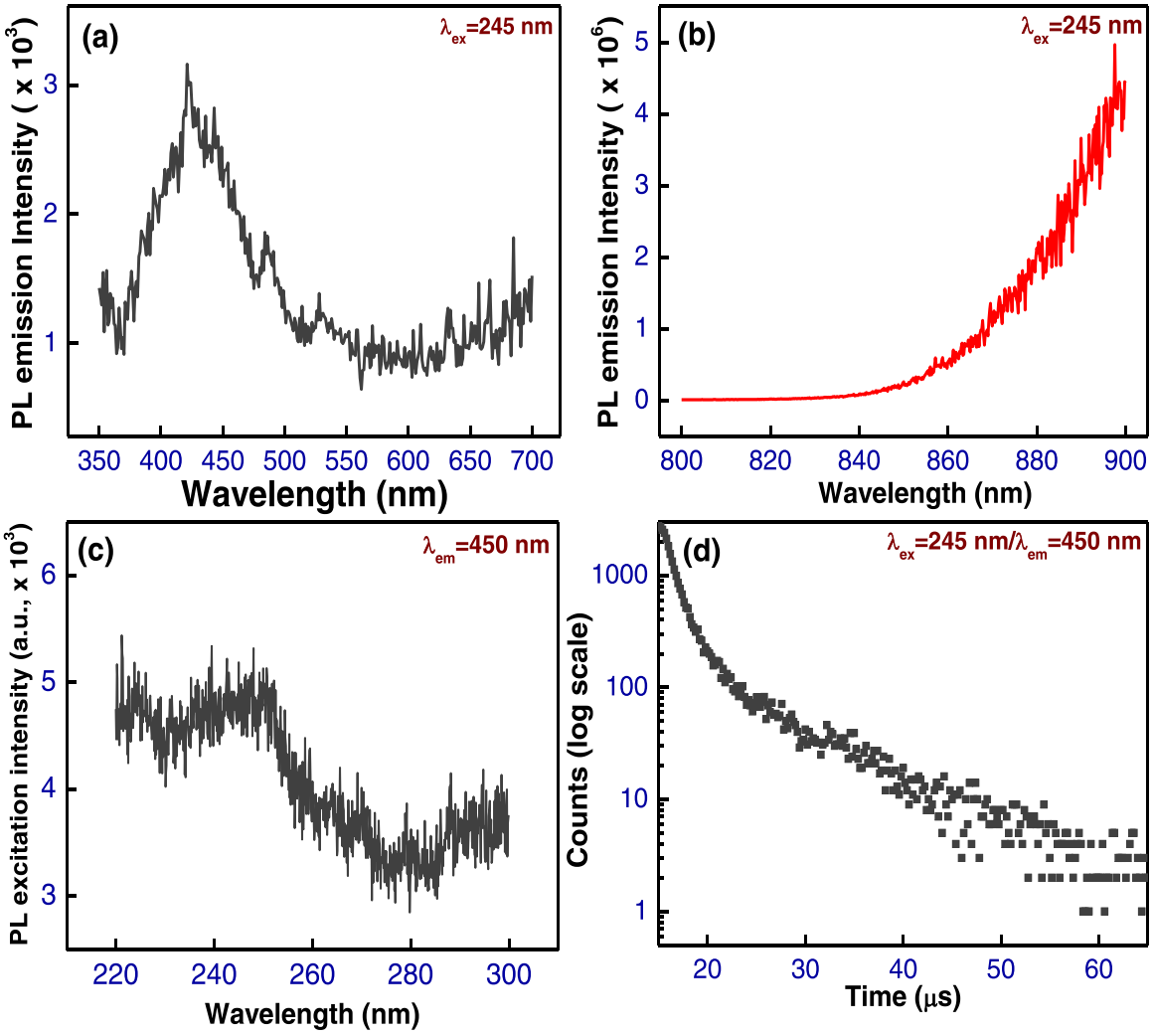

Fig. 8. (a) Emission (Visible range), (b) Emission (NIR range) (c) excitation and (d) lifetime spectra of aqueous suspension of MF sample.

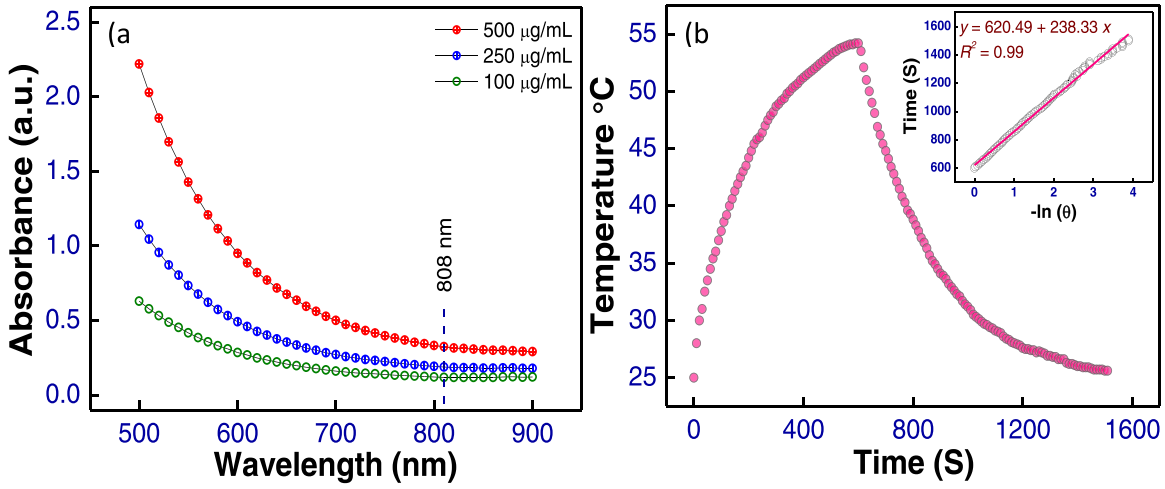

Fig. 9. (a) Concentration dependent UV–vis absorption spectra, and (b) heating and cooling curves for 500 μg/mL aqueous suspension under 0.33 W cm^{-2} laser irradiation.

recombination of electron-hole pair, generated during the excitation, could be increased by introducing the defect state in the material [38].

Photoluminescence measurements are shown in Fig. 8. The visible emission spectrum (Fig. 8*a)* of nano-crystalline $MnFe_2O_4$ under 245 nm excitation showed a prominent broad peak at around 430 nm and two smaller peaks at around 480 and 530 nm. In addition, several feeble peaks could be observed over 600–700 nm. Such multiple peaks are ascribed to the presence of several defect states in the band-gap of nano-crystalline $MnFe_2O_4$. Jacintha et al. [60] have also observed multiple PL band in the range 415–600 nm, and the same has been attributed to the presence of defects and oxygen vacancies (OVs). The OVs can be neutral, singly ionised or doubly ionised depending upon the formation energy [61,62]. Gupta et al. [61] have ascribed the blue bands at 423 and 483 nm to the transition from the conduction band to the defect state created by the presence of neutral OVs. While several authors have attributed the presence of a blue band in PL spectrum of $MnFe_2O_4$ to the radiative defects associated with interface traps existing at the grain boundaries [60,63,64]. This conclusion was followed after Jin et al. [65], which ascribed the violet luminescence at 420 nm to the radiative defects related to the interface traps existing at ZnO-ZnO grain boundaries. Nguyen et al. [66] have attributed the PL peak at 425 nm for Fe_3O_4 to the radiative recombination of the trapped electron from the octahedral sites to O 2p level. In fact, Nguyen et al. [66] and Sadat et al. [38] could propose the band-gap structure of Fe_3O_4 from PL measurements.

In $MnFe_2O_4$, the substitution of $Fe^{2+}/^{3+}$ ions at octahedral and tetrahedral sites by Mn^{2+}/Mn^{3+} ions is believed to modify the defect state and band structure. Here, a wide blue band centred around 430 nm (2.88 eV), which suggest the presence of various defect states, could arise due to radiative recombination of trapped electrons at the octahedral site to the photo-generated holes from the O 2p state [66]. A green band at 530 nm (2.33 eV) could refer to the radiative recombination of mobile electrons from, e_g to t_{2g} at the octahedral site [38,66]. In Fe_3O_4, the energy gap due to crystal field splitting at octahedral is ~ 2.2 eV [38]. In addition, a green band also appear due to radiative recombination of the photo-excited hole with electron trapped in singly ionised oxygen vacancies (F^+-centres) [64]. The feeble peaks observed over 600–700 nm (2.06–1.77 eV) could have stirred by the radiative recombination of trapped electrons from octahedral or crystal field (t_{2g}) on tetrahedral sites to the O 2p valence band [66].

NIR PL spectra of nanocrystalline MF altogether showed impressive results. Under 245 nm excitation, there is a progression of a very intense peak in the region of 800–900 nm (Fig. 8*b)* with a relative photon count of 10^6. The emission peak around ~ 870 nm can be attributed to the transitions of trapped electrons from one defect state to another in tetrahedral position. Sadat et al. [38] have observed NIR peak at around 840 nm in nano-crystalline Fe_3O_4 and ascribed the same to electron traps in OVs at the tetrahedral site. Due to the limitation of our instrument having a PMT detector that is sensitive up to 900 nm, further measurement was not possible. However, such an intense NIR peak is one reason for the excellent photo-thermal property of nano-crystalline MF.

The PL excitation spectrum (Fig. 8*c*), on the other hand, displayed a band around 245 nm, which can have the combined contribution from intrinsic $O^{2-} \rightarrow Fe^{3+}$ charge transfer as well as transition involving defect state [67]. Such a peculiar band in the UV region is typical of spinels [68]. The lifetime of the defect induced blue band in nano-crystalline MF is around 8.23 µs as obtained by mono-exponential fitting of luminescence decay profile shown in Fig. 8*d*. Such lifetime is typical of singly ionized OVs (also known as F^+ centres) found in spinels.

The Fig. 9*a* illustrates the concentration-dependent absorption behaviour for the aqueous MF suspension over a wavelength span of 500–900 nm. The suspensions displayed absorbance over the entire span, which decreased with increasing wavelength. In addition to the non-radiative relaxation process, the photo-thermal therapy is directly dependent on their NIR optical absorption efficiency. A finite absorbance near the NIR region, which was 0.324, 0.188 and 0.119 at concentration 500, 250 and 100 µg/mL, respectively, were observed for the suspension.

Fig. 9*b* shows the time-dependent heating and cooling cycle for the aqueous suspension of MF (500 µg/mL) after exposure to 808 nm NIR of 0.33 W cm^{-2} power density. A decay time of ~ 238 s was obtained from the analysis of the cooling cycle (inset Figure). The corresponding *hA* value was deduced to be 7.42 W/°C. The calculation of energy input based on the heat generated by the solvent is given elsewhere and found to be 3.56 mW at the power density of 0.33 W cm^{-2} [30]. The photo-thermal efficiency was found to be ~ 63% using relation 2 (Supplementary information). In our previous work [30], we found this efficiency to be ~ 70% for γ-Fe_2O_3 nano-flowers. Though the temperature achieved with MF was higher, its lower efficiency is due to its relatively higher absorbance at 808 nm. For IONPs with different coatings, Sadat et al. [38] had observed 'η' values ranging from ~ 16% to 76%, which portray the suitability of these MNPs as an alternative photo-thermal agent. Further, in-vitro studies were performed to evaluate the efficacy of these particles in cellular environment.

Confocal images show that uptake of MNPs by SiHa cells starts to appear after 30 min incubation and significant amounts of MNPs start to accumulate in cells after 5 h incubation (Fig. 10). Thus before PTT or MHT experiments we incubated the cells with magnetic material for 5 h. After 24 h of incubation nano-materials surrounded the nucleus of the cell. Higher magnification offers a better visualisation of the particles around the nucleus as shown in Fig. S4 (Supplementary file).

Calcein-AM and propidium iodide assays confirmed that there was no significant toxicity of MNPs in SiHa cells after 5 h incubation (Fig. 11). However, after PTT with MnFe2O4 nano-flowers for 10 mins using 808 nm laser of 0.66 W cm^{-2} power density the cell viability was significantly reduced (compared by one way ANOVA test). From the fluorescence microscopy the cell damage was apparent, increased propidium iodide signal, when treated with 500 µg/mL $MnFe_2O_4$ nano-flowers. (Fig. 12). The bright field image also shows the disruption of the cells. When treated with 250 µg/mL nano-flowers the cell viability decreased to ~ 74% after PTT, still the effect was found to be insignificant when compared with the viability of cells (~ 86%) after the exposure with nano-flowers alone. Thus, 500 µg/mL $MnFe_2O_4$ nano-flowers was essential to significantly reduce the viability of the cells through PTT. Also, the substantial effect could be produced with one-time treatment only. In comparison, the MHT did not induce significant toxicity to SiHa cells with 500 µg/mL MNFs treated for 10 min (Fig. S4). As depicted in (Fig. 6*b*), the temperature reached just 42 °C after the nano-flowers were exposed to AMF for 10 min which was not sufficient to induce damage to the cancer cells. Nevertheless, the heating ability of MNPs reduce in cell-environment as indicated by several authors. Thus, possibly longer treatment time or higher concentration of MnFe2O4 nano-flowers would be required to induce toxicity through MHT. For example MHT treatment of HeLa cells with 0.75 mg/mL material for 30 min could reduce the viability to 17% [69]. Gupta et al. [70] demonstrated a significant reduction in cell viability (C6 cells) after a subsequent PTT and MHT.

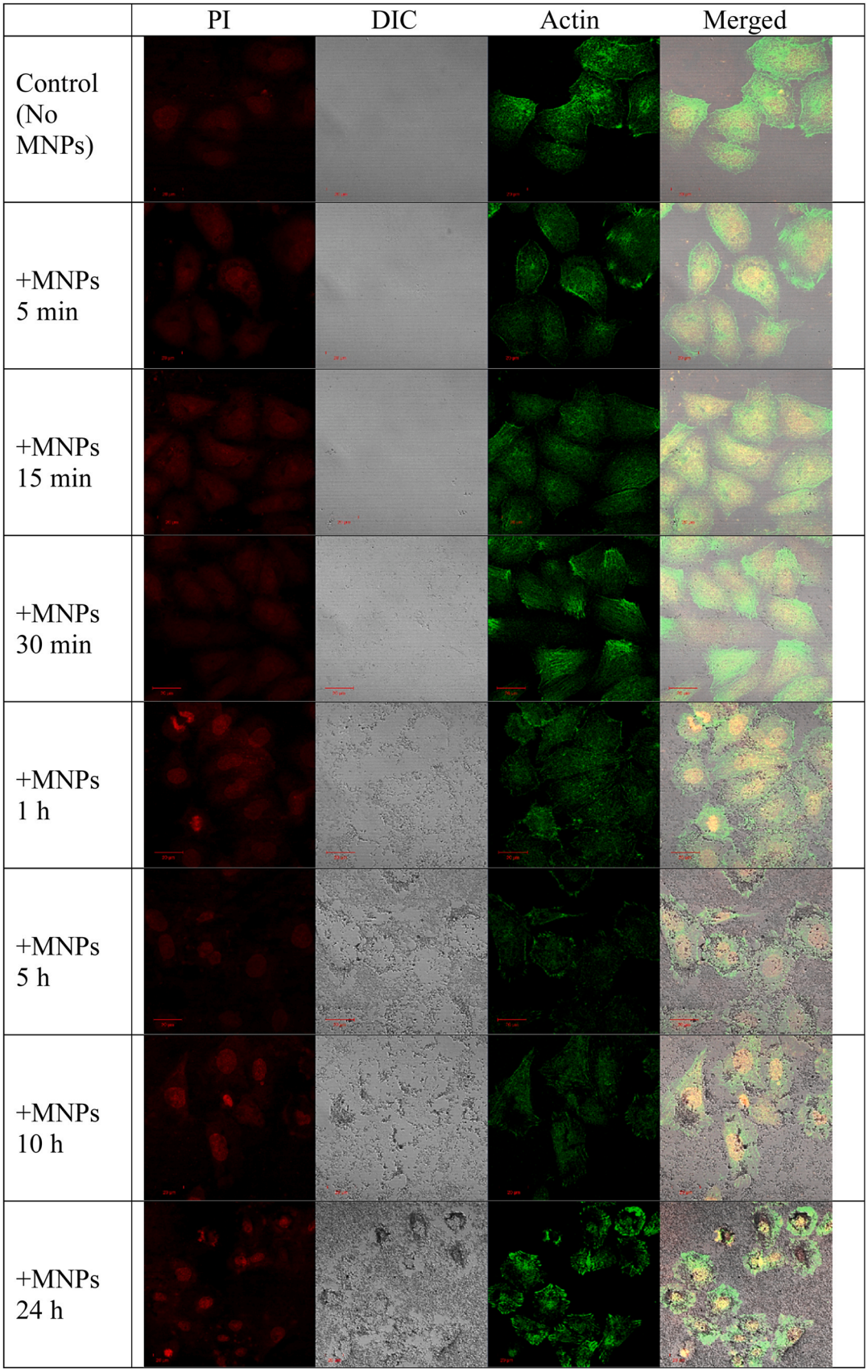

Fig. 10. Confocal microscopy images showing SiHa cells stained with phalloidin (green, for actin in cytoplasm) and propidium iodide (red, for nucleus) with and without MNPs incubation at different time intervals.

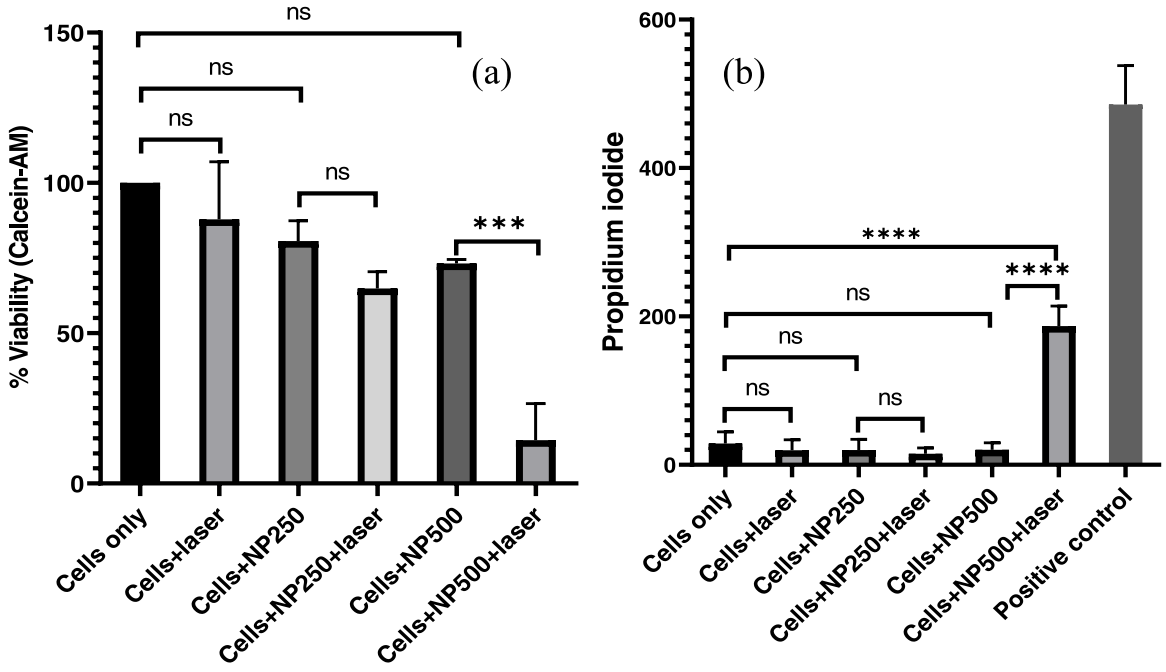

Fig. 11. (a) Calcein-AM and (b) propidium iodide assays of SiHa cells with and without MNPs and PTH (laser treatment); ns: not significant, ***:$p \leq 0.001$, ****:$p \leq 0.0001$.

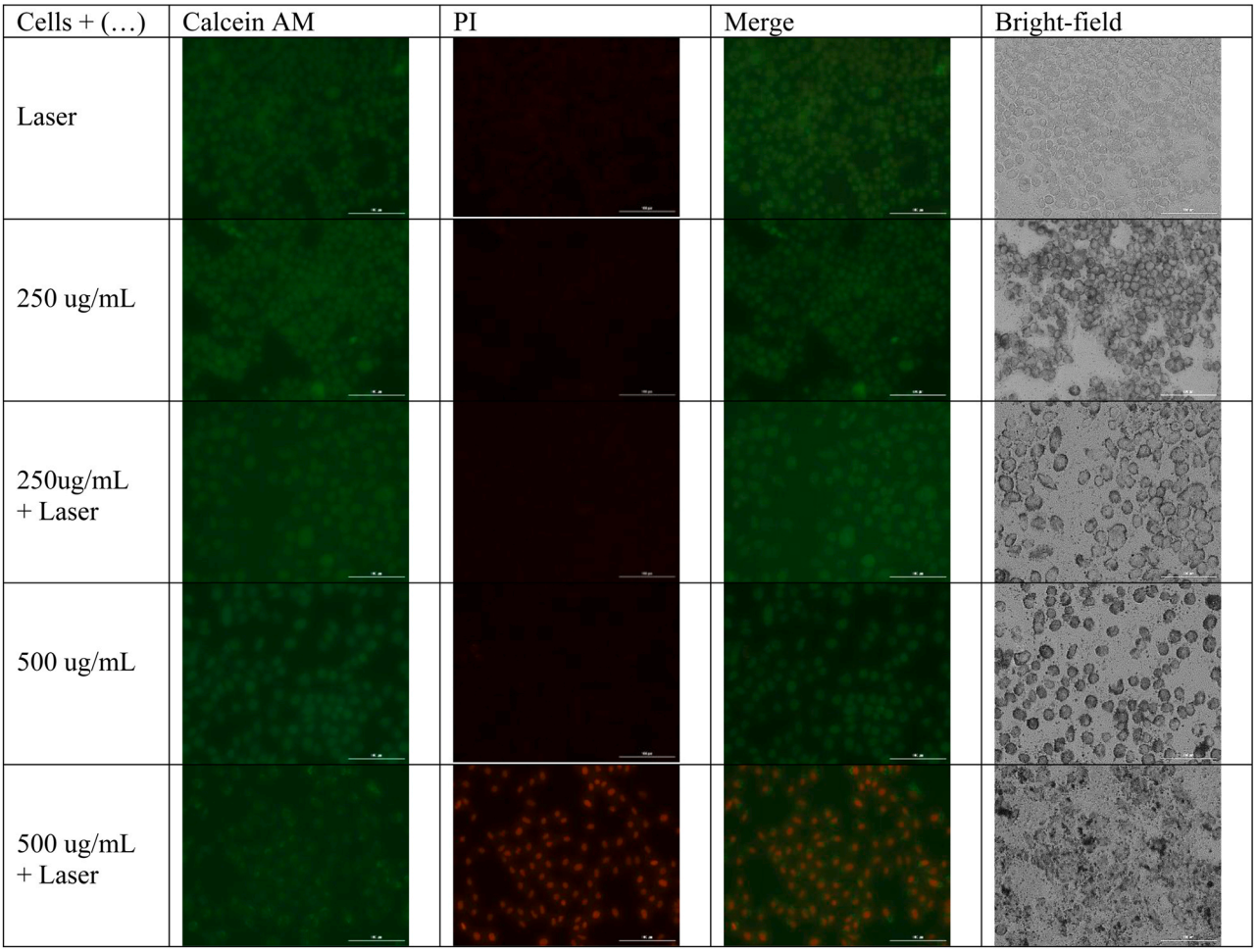

Fig. 12. Fluorescence microscopy images showing SiHa cells stained with Calcein-AM (green, live cells) and propidium iodide (red, dead cells) after PTT.

3. Conclusion

We have successfully synthesised $MnFe_2O_4$ nano-flowers via solvo-thermal process which was confirmed from XRD, XPS, TEM and Mössbauer spectroscopy. The nano-flowers displayed improved saturation magnetisation owing to the reduced surface disorder and possible magnetic ordering within the flowers. The highest ILP value of 5.31 ± 0.079 nH m^2 kg^{-1} observed at an AMF of amplitude 170 Oe and frequency 330 kHz is comparable to the values for Fe_3O_4 nano-flowers reported earlier. The material showed a very high heating capability under NIR irradiation of low power density. The intense NIR photo-counts is one reason for their excellent photo-thermal performance. The aqueous suspension of the nano-flowers showed good absorbance near NIR region and a photo-thermal conversion efficiency of ~63%. Under NIR irradiation the therapeutic temperature (~42–46 °C) was achievable even at a low concentration of 100 μg/mL. It makes the current MF sample as a prospective photo-thermal agent. The present in-vitro studies suggest that the MF could internalise in the cells. Hence, high rate of cells death was noticed during PTT even at a concentration as low as 500 μg/mL for an exposure time of only 10 min. In contrast, MHT at this concentration and at a similar exposure time, could not cause cells death due to lesser achieved temperature (~42 °C). This validate better efficacy of PTT amongst the two modalities. Nevertheless, higher temperature required for cells death could be achieved during MHT either by enhancing the concentration of MF or the duration of exposure.

CRediT authorship contribution statement

S.K. Shaw: Conceptualization, Methodology, Formal analysis, Investigation, Data curation, Writing – original draft. **J. Kailashiya:** Formal analysis, Investigation, Data curation, Writing – review & editing. **Santosh K. Gupta:** Formal analysis, Investigation, Data curation, Writing – review & editing. **C.L. Prajapat:** Formal analysis, Investigation. **Sher Singh Meena:** Formal analysis, Writing – review & editing. **D. Dash:** Writing – review & editing, Supervision, Funding acquisition. **P. Maiti:** Writing – review & editing, Supervision. **N.K. Prasad:** Conceptualization, Writing – review & editing, Supervision, Project administration, Funding acquisition.

Declaration of Competing Interest

The authors declare that they have no known competing financial interests or personal relationships that could have appeared to influence the work reported in this paper.

Acknowledgement

N. K. Prasad would like to thank the Department of Science and Technology for sponsored project CRG/2019/000176 for partial financial assistance. Part of this research was supported by grants received by D. Dash from the Indian Council of Medical Research (ICMR) under CAR scheme (71/4/2018-BMS-CAR) and J. C. Bose National Fellowship (SERB) grant (JCB/2017/000029).

Appendix A. Supporting information

Supplementary data associated with this article can be found in the online version at doi:10.1016/j.jallcom.2021.163192.

References

[1] R.L. Siegel, K.D. Miller, H.E. Fuchs, A. Jemal, Cancer statistics, 2021, CA: a Cancer J. Clin. 71 (1) (2021) 7–33.
[2] P. Mathur, K. Sathishkumar, M. Chaturvedi, P. Das, K.L. Sudarshan, S. Santhappan, V. Nallasamy, A. John, S. Narasimhan, F.S. Roselind, ICMR-NCDIR-NCRP Investigator Group, Cancer statistics, 2020: report from national cancer registry programme, India, JCO Glob. Oncol. 6 (2020) 1063–1075.
[3] P. Angsutararux, S. Luanpitpong, S. Issaragrisil, Chemotherapy-induced cardiotoxicity: overview of the roles of oxidative stress, Oxid. Med. Cell. Longev. (2015) 795602.
[4] C. Yarana, D.K. St Clair, Chemotherapy-induced tissue injury: an insight into the role of extracellular vesicles-mediated oxidative stress responses, Antioxidants 6 (4) (2017) 75.
[5] S.K. Sharma, N. Shrivastava, F. Rossi, N.T.K. Thanh, Nanoparticles-based magnetic and photo induced hyperthermia for cancer treatment, Nano Today 29 (2019) 100795.
[6] Y. Xiao, J. Du, Superparamagnetic nanoparticles for biomedical applications, J. Mater. Chem. B 8 (3) (2020) 354–367.
[7] L.L. Israel, A. Galstyan, E. Holler, J.Y. Ljubimova, Magnetic iron oxide nanoparticles for imaging, targeting and treatment of primary and metastatic tumors of the brain, J. Control. Release 320 (2020) 45–62.
[8] T. Vangijzegem, D. Stanicki, S. Laurent, Magnetic iron oxide nanoparticles for drug delivery: applications and characteristics, Expert Opin. Drug Deliv. 16 (1) (2019) 69–78.
[9] H. Al Faruque, E.S. Choi, H.R. Lee, J.H. Kim, S. Park, E. Kim, Targeted removal of leukemia cells from the circulating system by whole-body magnetic hyperthermia in mice, Nanoscale 12 (4) (2020) 2773–2786.
[10] Y.X.J. Wáng, J.M. Idée, A comprehensive literatures update of clinical researches of superparamagnetic resonance iron oxide nanoparticles for magnetic resonance imaging, Quant. Imaging Med. Surg. 7 (1) (2017) 88.
[11] L.M. Bauer, S.F. Situ, M.A. Griswold, A.C.S. Samia, High-performance iron oxide nanoparticles for magnetic particle imaging–guided hyperthermia (hMPI), Nanoscale 8 (24) (2016) 12162–12169.
[12] D. Ortega, Q.A. Pankhurst, Magnetic hyperthermia, Nanoscience 1 (60) (2013) e88.
[13] J. Carrey, B. Mehdaoui, M. Respaud, Simple models for dynamic hysteresis loop calculations of magnetic single-domain nanoparticles: application to magnetic hyperthermia optimization, J. Appl. Phys. 109 (8) (2011) 083921.
[14] Z. Nemati, J. Alonso, I. Rodrigo, R. Das, E. Garaio, J.Á. García, I. Orue, M.H. Phan, H. Srikanth, Improving the heating efficiency of iron oxide nanoparticles by tuning their shape and size, J. Phys. Chem. C 122 (4) (2018) 2367–2381.
[15] S. Laurent, S. Dutz, U.O. Häfeli, M. Mahmoudi, Magnetic fluid hyperthermia: focus on superparamagnetic iron oxide nanoparticles, Adv. Colloid Interface Sci. 166 (1–2) (2011) 8–23.
[16] M. Jeun, S. Lee, J. Kyeong Kang, A. Tomitaka, K. Wook Kang, Y. Il Kim, Y. Takemura, K.W. Chung, J. Kwak, S. Bae, Physical limits of pure superparamagnetic Fe_3O_4 nanoparticles for a local hyperthermia agent in nanomedicine, Appl. Phys. Lett. 100 (9) (2012) 092406.
[17] L. Kafrouni, O. Savadogo, Recent progress on magnetic nanoparticles for magnetic hyperthermia, Prog. Biomater. 5 (3) (2016) 147–160.
[18] Z. Nemati, J. Alonso, L.M. Martinez, H. Khurshid, E. Garaio, J.A. Garcia, M.H. Phan, H. Srikanth, Enhanced magnetic hyperthermia in iron oxide nano-octopods: size and anisotropy effects, J. Phys. Chem. C 120 (15) (2016) 8370–8379.
[19] S.H. Noh, W. Na, J.T. Jang, J.H. Lee, E.J. Lee, S.H. Moon, Y. Lim, J.S. Shin, J. Cheon, Nanoscale magnetism control via surface and exchange anisotropy for optimized ferrimagnetic hysteresis, Nano Lett. 12 (7) (2012) 3716–3721.
[20] P. Hugounenq, M. Levy, D. Alloyeau, L. Lartigue, E. Dubois, V. Cabuil, C. Ricolleau, S. Roux, C. Wilhelm, F. Gazeau, R. Bazzi, Iron oxide monocrystalline nanoflowers for highly efficient magnetic hyperthermia, J. Phys. Chem. C 116 (29) (2012) 15702–15712.
[21] P. Kowalik, J. Mikulski, A. Borodziuk, M. Duda, I. Kamińska, K. Zajdel, J. Rybusinski, J. Szczytko, T. Wojciechowski, K. Sobczak, R. Minikayev, Yttrium-doped iron oxide nanoparticles for magnetic hyperthermia applications, J. Phys. Chem. C 124 (12) (2020) 6871–6883.
[22] X. Yu, L. Wang, K. Li, Y. Mi, Z. Li, F. Sun, S. He, H. Zeng, Tuning dipolar effects on magnetic hyperthermia of $Zn_{0.3}Fe_{2.7}O_4/SiO_2$ nanoparticles by silica shell, J. Magn. Magn. Mater. 521 (2021) 167483.
[23] P. Bender, J. Fock, C. Frandsen, M.F. Hansen, C. Balceris, F. Ludwig, O. Posth, E. Wetterskog, L.K. Bogart, P. Southern, W. Szczerba, Relating magnetic properties and high hyperthermia performance of iron oxide nanoflowers, J. Phys. Chem. C 122 (5) (2018) 3068–3077.
[24] C. Blanco-Andujar, D. Ortega, P. Southern, Q.A. Pankhurst, N.T.K. Thanh, High performance multi-core iron oxide nanoparticles for magnetic hyperthermia: microwave synthesis, and the role of core-to-core interactions, Nanoscale 7 (5) (2015) 1768–1775.
[25] S. Sabale, V. Jadhav, V. Khot, X. Zhu, M. Xin, H. Chen, Superparamagnetic MFe_2O_4 (M = Ni, Co, Zn, Mn) nanoparticles: synthesis, characterization, induction heating and cell viability studies for cancer hyperthermia applications, J. Mater. Sci.: Mater. Med. 26 (3) (2015) 127.
[26] P. Pradhan, J. Giri, G. Samanta, H.D. Sarma, K.P. Mishra, J. Bellare, R. Banerjee, D. Bahadur, Comparative evaluation of heating ability and biocompatibility of different ferrite-based magnetic fluids for hyperthermia application, J. Biomed. Mater. Res. Part B: Appl. Biomater.: Off. J. Soc. Biomater. Jpn. Soc. Biomater. Aust. Soc. Biomater. Korean Soc. Biomater. 81 (1) (2007) 12–22.
[27] G. Hemery, A.C. Keyes Jr., E. Garaio, I. Rodrigo, J.A. Garcia, F. Plazaola, E. Garanger, O. Sandre, Tuning sizes, morphologies, and magnetic properties of monocore versus multicore iron oxide nanoparticles through the controlled addition of water in the polyol synthesis, Inorg. Chem. 56 (14) (2017) 8232–8243.

[28] L. Lartigue, P. Hugounenq, D. Alloyeau, S.P. Clarke, M. Levy, J.C. Bacri, R. Bazzi, D.F. Brougham, C. Wilhelm, F. Gazeau, Cooperative organization in iron oxide multi-core nanoparticles potentiates their efficiency as heating mediators and MRI contrast agents, ACS Nano 6 (12) (2012) 10935–10949.
[29] G. Kandasamy, S. Khan, J. Giri, S. Bose, N.S. Veerapu, D. Maity, One-pot synthesis of hydrophilic flower-shaped iron oxide nanoclusters (IONCs) based ferrofluids for magnetic fluid hyperthermia applications, J. Mol. Liq. 275 (2019) 699–712.
[30] S.K. Shaw, J. Kailashiya, A. Gangwar, S.K. Alla, S.K. Gupta, C.L. Prajapat, S.S. Meena, D. Dash, P. Maiti, N.K. Prasad, γ-Fe_2O_3 nanoflowers as efficient magnetic hyperthermia and photothermal agent, Appl. Surf. Sci. (2021) 150025.
[31] A. Espinosa, R. Di Corato, J. Kolosnjaj-Tabi, P. Flaud, T. Pellegrino, C. Wilhelm, Duality of iron oxide nanoparticles in cancer therapy: amplification of heating efficiency by magnetic hyperthermia and photothermal bimodal treatment, ACS Nano 10 (2) (2016) 2436–2446.
[32] N.S. Abadeer, C.J. Murphy, Recent progress in cancer thermal therapy using gold nanoparticles, J. Phys. Chem. C 120 (9) (2016) 4691–4716.
[33] X. Liu, H. Tao, K. Yang, S. Zhang, S.T. Lee, Z. Liu, Optimization of surface chemistry on single-walled carbon nanotubes for in vivo photothermal ablation of tumors, Biomaterials 32 (1) (2011) 144–151.
[34] W. Zhang, Z. Guo, D. Huang, Z. Liu, X. Guo, H. Zhong, Synergistic effect of chemo-photothermal therapy using PEGylated graphene oxide, Biomaterials 32 (33) (2011) 8555–8561.
[35] C. Lopez-Chaves, J. Soto-Alvaredo, M. Montes-Bayon, J. Bettmer, J. Llopis, C. Sanchez-Gonzalez, Gold nanoparticles: distribution, bioaccumulation and toxicity. In vitro and in vivo studies, Nanomed.: Nanotechnol. Biol. Med. 14 (1) (2018) 1–12.
[36] D. Mateo, P. Morales, A. Ávalos, A.I. Haza, Oxidative stress contributes to gold nanoparticle-induced cytotoxicity in human tumor cells, Toxicol. Mech. Methods 24 (3) (2014) 161–172.
[37] A. Espinosa, J. Kolosnjaj-Tabi, A. Abou-Hassan, A. Plan Sangnier, A. Curcio, A.K. Silva, R. Di Corato, S. Neveu, T. Pellegrino, L.M. Liz-Marzán, C. Wilhelm, Magnetic (hyper) thermia or photothermia? Progressive comparison of iron oxide and gold nanoparticles heating in water, in cells, and in vivo, Adv. Funct. Mater. 28 (37) (2018) 1803660.
[38] M.E. Sadat, M. Kaveh Baghbador, A.W. Dunn, H.P. Wagner, R.C. Ewing, J. Zhang, H. Xu, G.M. Pauletti, D.B. Mast, D. Shi, Photoluminescence and photothermal effect of Fe_3O_4 nanoparticles for medical imaging and therapy, Appl. Phys. Lett. 105 (9) (2014) 091903.
[39] S. Shen, S. Wang, R. Zheng, X. Zhu, X. Jiang, D. Fu, W. Yang, Magnetic nanoparticle clusters for photothermal therapy with near-infrared irradiation, Biomaterials 39 (2015) 67–74.
[40] M. Saeed, M.Z. Iqbal, W. Ren, Y. Xia, C. Liu, W.S. Khan, A. Wu, Controllable synthesis of Fe_3O_4 nanoflowers: enhanced imaging guided cancer therapy and comparison of photothermal efficiency with black-TiO2, J. Mater. Chem. B 6 (22) (2018) 3800–3810.
[41] B. Aslibeiki, P. Kameli, H. Salamati, The effect of dipole-dipole interactions on coercivity, anisotropy constant, and blocking temperature of $MnFe_2O_4$ nanoparticles, J. Appl. Phys. 119 (6) (2016) 063901.
[42] I. Corazzari, R. Nisticò, F. Turci, M.G. Faga, F. Franzoso, S. Tabasso, G. Magnacca, Advanced physico-chemical characterization of chitosan by means of TGA coupled on-line with FTIR and GCMS: thermal degradation and water adsorption capacity, Polym. Degrad. Stab. 112 (2015) 1–9.
[43] M. Karegar, M.M. Khodaei, Synthesis of Fe_3O_4-PVP nanocomposite functionalized with sulfonic group as an effective catalyst for one-pot synthesis of xanthene derivatives, Res. Chem. Intermed. 47 (11) (2021) 4537–4555.
[44] T. Yamashita, P. Hayes, Analysis of XPS spectra of Fe^{2+} and Fe^{3+} ions in oxide materials, Appl. Surf. Sci. 254 (8) (2008) 2441–2449.
[45] A.P. Grosvenor, B.A. Kobe, M.C. Biesinger, N.S. McIntyre, Investigation of multiplet splitting of Fe 2p XPS spectra and bonding in iron compounds, Surf. Interface Anal.: Int. J. Devoted Dev. Appl. Tech. Anal. Surf. Interfaces Thin Films 36 (12) (2004) 1564–1574.
[46] D. Wilson, M.A. Langell, XPS analysis of oleylamine/oleic acid capped Fe_3O_4 nanoparticles as a function of temperature, Appl. Surf. Sci. 303 (2014) 6–13.
[47] S. Poulin, R. Franca, L. Moreau-Bélanger, E. Sacher, Confirmation of X-ray photoelectron spectroscopy peak attributions of nanoparticulate iron oxides, using symmetric peak component line shapes, J. Phys. Chem. C 114 (24) (2010) 10711–10718.
[48] A.M.E. Raj, S.G. Victoria, V.B. Jothy, C. Ravidhas, J. Wollschläger, M. Suendorf, M. Neumann, M. Jayachandran, C. Sanjeeviraja, XRD and XPS characterization of mixed valence Mn_3O_4 hausmannite thin films prepared by chemical spray pyrolysis technique, Appl. Surf. Sci. 256 (9) (2010) 2920–2926.
[49] S.K. Shaw, A. Gangwar, A. Sharma, S.K. Alla, S. Kavita, M. Vasundhara, S.S. Meena, P. Maiti, N.K. Prasad, Structural and magnetic properties of nanocrystalline equiatomic spinel high-entropy oxide $(AlCoFeMnNi)_3O_4$ synthesised by microwave assisted co-precipitation technique, J. Alloy. Compd. 878 (2021) 160269.
[50] A.L. Tiano, G.C. Papaefthymiou, C.S. Lewis, J. Han, C. Zhang, Q. Li, C. Shi, A.M. Abeykoon, S.J. Billinge, E. Stach, J. Thomas, Correlating size and composition-dependent effects with magnetic, mossbauer, and pair distribution function measurements in a family of catalytically active ferrite nanoparticles, Chem. Mater. 27 (10) (2015) 3572–3592.
[51] R. Topkaya, H. Güngüneş, Ş. Eryiğit, S.E. Shirsath, A. Yıldız, A. Baykal, Effect of bimetallic (Ni and Co) substitution on magnetic properties of $MnFe_2O_4$ nanoparticles, Ceram. Int. 42 (12) (2016) 13773–13782.
[52] I.N. Zakharova, M.A. Shipilin, V.P. Alekseev, A.M. Shipilin, Mössbauer study of maghemite nanoparticles, Tech. Phys. Lett. 38 (1) (2012) 55–58.
[53] M.A.N.M.B. Siddique, N.M. Butt, Effect of particle size on degree of inversion in ferrites investigated by Mössbauer spectroscopy, Phys. B: Condens. Matter 405 (19) (2010) 4211–4215.
[54] E.C. Abenojar, S. Wickramasinghe, J. Bas-Concepcion, A.C.S. Samia, Structural effects on the magnetic hyperthermia properties of iron oxide nanoparticles, Prog. Nat. Sci.: Mater. Int. 26 (5) (2016) 440–448.
[55] B. Mehdaoui, R.P. Tan, A. Meffre, J. Carrey, S. Lachaize, B. Chaudret, M. Respaud, Increase of magnetic hyperthermia efficiency due to dipolar interactions in low-anisotropy magnetic nanoparticles: theoretical and experimental results, Phys. Rev. B 87 (17) (2013) 174419.
[56] P. Bender, D. Honecker, L. Fernández Barquín, Supraferromagnetic correlations in clusters of magnetic nanoflowers, Appl. Phys. Lett. 115 (13) (2019) 132406.
[57] R.E. Rosensweig, Heating magnetic fluid with alternating magnetic field, J. Magn. Magn. Mater. 252 (2002) 370–374.
[58] T. Yamaminami, S. Ota, S.B. Trisnanto, M. Ishikawa, T. Yamada, T. Yoshida, K. Enpuku, Y. Takemura, Power dissipation in magnetic nanoparticles evaluated using the AC susceptibility of their linear and nonlinear responses, J. Magn. Magn. Mater. 517 (2021) 167401.
[59] C.J. Bae, S. Angappane, J.G. Park, Y. Lee, J. Lee, K. An, T. Hyeon, Experimental studies of strong dipolar interparticle interaction in monodisperse Fe_3O_4 nanoparticles, Appl. Phys. Lett. 91 (10) (2007) 102502.
[60] A.M. Jacintha, A. Manikandan, K. Chinnaraj, S.A. Antony, P. Neeraja, Comparative studies of spinel $MnFe_2O_4$ nanostructures: structural, morphological, optical, magnetic and catalytic properties, J. Nanosci. Nanotechnol. 15 (12) (2015) 9732–9740.
[61] S.K. Gupta, K. Sudarshan, B. Modak, A.K. Yadav, P. Modak, S.N. Jha, D. Bhattacharyya, Achieving bright blue and red luminescence in Ca_2SnO_4 through defect and doping manipulation, J. Phys. Chem. C 124 (29) (2020) 16090–16101.
[62] S.K. Gupta, J.P. Zuniga, M. Abdou, P.S. Ghosh, Y. Mao, Optical properties of undoped, Eu^{3+} doped and Li^+ co-doped $Y_2Hf_2O_7$ nanoparticles and polymer nanocomposite films, Inorg. Chem. Front. 7 (2) (2020) 505–518.
[63] A.M. Jacintha, V. Umapathy, P. Neeraja, S.R.J. Rajkumar, Synthesis and comparative studies of $MnFe_2O_4$ nanoparticles with different natural polymers by sol–gel method: structural, morphological, optical, magnetic, catalytic and biological activities, J. Nanostruct. Chem. 7 (4) (2017) 375–387.
[64] J.J. Vijaya, G. Sekaran, M. Bououdina, Effect of Cu^{2+} doping on structural, morphological, optical and magnetic properties of $MnFe_2O_4$ particles/sheets/flakes-like nanostructures, Ceram. Int. 41 (1) (2015) 15–26.
[65] B.J. Jin, S. Im, S.Y. Lee, Violet and UV luminescence emitted from ZnO thin films grown on sapphire by pulsed laser deposition, Thin Solid Films 366 (1–2) (2000) 107–110.
[66] H.H. Nguyen, H.K.T. Ta, S. Park, T.B. Phan, N.K. Pham, Resistive switching effect and magnetic properties of iron oxide nanoparticles embedded-polyvinyl alcohol film, RSC Adv. 10 (22) (2020) 12900–12907.
[67] J. Zaanen, G.A. Sawatzky, J.W. Allen, Band gaps and electronic structure of transition-metal compounds, Phys. Rev. Lett. 55 (4) (1985) 418.
[68] B.B. Srivastava, S.K. Gupta, Y. Mao, Remarkable enhancement of photoluminescence and persistent luminescence of NIR emitting $ZnGa_2O_4$: Cr^{3+} nanoparticles, CrystEngComm 22 (14) (2020) 2491–2501.
[69] S.K. Shaw, A. Biswas, A. Gangwar, P. Maiti, C.L. Prajapat, S.S. Meena, N.K. Prasad, Synthesis of exchange coupled nanoflowers for efficient magnetic hyperthermia, J. Magn. Magn. Mater. 484 (2019) 437–444.
[70] R. Gupta, D. Sharma, Manganese-doped magnetic nanoclusters for hyperthermia and photothermal glioblastoma therapy, ACS Appl. Nano Mater. 3 (2) (2020) 2026–2037.